ACS APPLIED MATERIALS & INTERFACES

Research Article

www.acsami.org

Stimulation of Electro-oxidation Catalysis by Bulk-Structural Transformation in Intermetallic $ZrPt_3$ Nanoparticles

Gubbala V. Ramesh,*[,†] Rajesh Kodiyath,[†] Toyokazu Tanabe,[†] Maidhily Manikandan,[†,‡] Takeshi Fujita,[§,⊥] Naoto Umezawa,[†,⊥] Shigenori Ueda,[○] Shinsuke Ishihara,[∥] Katsuhiko Ariga,[∥,⊥] and Hideki Abe*[,†,⊥]

[†]National Institute for Materials Science, 1-1 Namiki, Tsukuba, Ibaraki 305-0044, Japan

[‡]Crystal Growth Centre, Anna University, Chennai, Tamil Nadu 600-025, India

[⊥]Precursory Research for Embryonic Science and Technology (PRESTO) and Core Research for Evolutionary Science and Technology (CREST), Japan Science and Technology Agency (JST), 4-1-8 Honcho, Kawaguchi, Saitama 332-0012, Japan

[§]WPI Advanced Institute for Materials Research, Tohoku University, Sendai 980-8577, Japan

[○]Synchrotron X-ray Station at SPring-8, National Institute for Materials Science, 1-1-1 Kouto, Sayo, Hyogo 679-5148, Japan

[∥]WPI International Center for Material Nanoarchitectonics, National Institute for Materials Science, 1-1 Namiki, Tsukuba, Ibaraki 305-0044, Japan

Supporting Information

ABSTRACT: Although compositional tuning of metal nanoparticles (NPs) has been extensively investigated, possible control of the catalytic performance through bulk-structure tuning is surprisingly overlooked. Here we report that the bulk structure of intermetallic $ZrPt_3$ NPs can be engineered by controlled annealing and their catalytic performance is significantly enhanced as the result of bulk-structural transformation. Chemical reduction of organometallic precursors yielded the desired $ZrPt_3$ NPs with a cubic FCC-type structure (*c*-$ZrPt_3$ NPs). The *c*-$ZrPt_3$ NPs were then transformed to a different phase of $ZrPt_3$ with a hexagonal structure (*h*-$ZrPt_3$ NPs) by annealing at temperatures between 900 and 1000 °C. The *h*-$ZrPt_3$ NPs exhibited higher catalytic activity and long-term stability than either the *c*-$ZrPt_3$ NPs or commercial Pt/C NPs toward the electro-oxidation of ethanol. Theoretical calculations have elucidated that the enhanced activity of the *h*-$ZrPt_3$ NPs is attributed to the increased surface energy, whereas the stability of the catalyst is retained by the lowered bulk-free-energy.

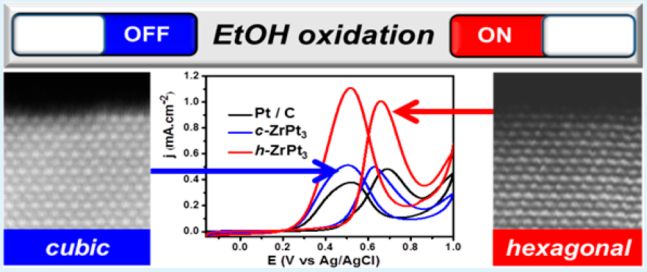

KEYWORDS: *catalysts, intermetallic compounds, bulk structural transformation, surface energy, polymer membrane electrolyte fuel cells*

1. INTRODUCTION

The increasing interest in renewable energies has highlighted the centrality of catalytic metal nanoparticles (NPs) in sustainable energy-conversion technologies including photocatalytic water splitting and polymer-electrolyte membrane fuel cells (PEMFCs).[1−6] In particular, confocal attention has been paid to alloy NPs consisting of platinum-group-metals (PGMs) and transition metals or metalloids which exhibit high catalytic performance compared with the NPs of prestine PGMs.[7−9] $NiPt_3$ and $CoPt_3$ NPs are highly active toward the electroreduction of oxygen (ORR).[10,11] $SnPt_3$, $CuPt_3$, and Ru−Pt NPs show good activity toward the electro-oxidation of small organic molecules such as methanol.[12−14] Currently, most of the catalytic functionalities of alloy NPs are controlled only through the alloy composition, where the constituent atoms are distributed on the crystal lattice of the FCC-type- or FCC-derivative structures.[15−19] Possible control of the catalytic performance of alloys through bulk-structure tuning has not been fully explored except for some pioneering works,[20−23] although a variety of functionalities of alloys, such as martensitic hardening and shape-memory effects,[24−26] significantly depend on the bulk structure and can be controlled by promoting bulk-structural transformation through external stimuli: pressure, temperature, and magnetic fields. Rational promotion of bulk-structural transformation of alloy NPs could realize enhanced activity and long-term stability, which are often mutually exclusive, because the bulk structure is not sensitive to surface segregation or impurity poisoning that degrades catalytic/sensing performance of the surface.[27] Herein, we report that the catalytic performance of alloy NPs can be significantly enhanced by promoting bulk-structural transformation (Scheme 1). We have synthesized NPs of an ordered alloy (intermetallic compound) of an early *d*-metal and Pt, $ZrPt_3$ ($ZrPt_3$ NPs), and tailored their bulk structure by

Received: June 26, 2014
Accepted: September 3, 2014
Published: September 3, 2014

Scheme 1. Transformation of $ZrPt_3$ NPs from Cubic to Hexagonal Bulk Structures, Resulting in Activation of Fuel-Oxidation Catalysis on the Surface

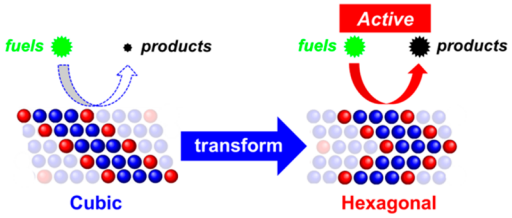

controlled annealing. It is known that the bulk structure of Zr-based alloys is sensitive to external stimuli such as pressure or temperature, often exhibiting shape-memory effects.[28] We have demonstrated that a temperature-induced structural transformation in the $ZrPt_3$ NPs from cubic to hexagonal structures lowers the bulk free energy and, in turn, elevates the surface energy. The catalytic activity and stability of the $ZrPt_3$ NPs are significantly enhanced through the structural transformation, as the result of the elevated surface energy and the lowered bulk free energy.

The $ZrPt_3$ NPs with the cubic $AuCu_3$-type structure (*c*-$ZrPt_3$ NPs, $Fm\bar{3}m$, a = 0.399 nm) were synthesized by coreduction of dichloro-(1,5-cyclooctadiene) platinum(II) and zirconium(IV) tetrachloride (see the Supporting Information for the synthetic details).[29] The *c*-$ZrPt_3$ NPs were then structurally transformed to hexagonally ordered *h*-$ZrPt_3$ NPs (space group $P6_3/mmc$, a = 0.562 nm, c = 0.921 nm) with the $TiNi_3$-type structure by vacuum annealing at 1000 °C.[30] Importantly, the *h*-$ZrPt_3$ NPs exhibited better catalytic performance than either the *c*-$ZrPt_3$ NPs or the commercial carbon-supported Pt NPs (Pt/C), in terms of stability to repeated electrochemical cycles and electrocatalytic activity toward the oxidation of ethanol. Theoretical calculations have elucidated that the structural transformation significantly increases the surface energy, which results in the enhanced catalytic performance of the *h*-$ZrPt_3$ NPs.

2. EXPERIMENTAL DETAILS

2.1. Materials. All the chemicals were used as purchased without further purification. Dichloro-(1,5-cyclooctadiene) platinum(II) (Pt(COD)Cl_2), zirconium(IV) chloride ($ZrCl_4$, anhydrous powder, 99.995% trace metals basis), superhydride solution ($LiEt_3BH$, 1.0 M in dry tetrahydrofuran (THF)) were purchased from Sigma-Aldrich. Diethylene glycol dimethyl ether (diglyme, anhydrous, 99.5%) and hexane (anhydrous, 95%) were also purchased from Sigma-Aldrich. The chemicals and solvents were always treated in a dry Ar atmosphere. Pt/C (20% mass loading) catalyst was obtained from Fuel Cell Store.

2.2. Methods. *2.2.1. Synthesis of Zr–Pt Alloy and $ZrPt_3$ Intermetallic Nanoparticles.* An aliquot of 0.12 mmol of the Pt precursor (Pt(COD)Cl_2) and 0.04 mmol of the Zr precursor ($ZrCl_4$) were dissolved in 30 mL of diglyme in an Ar atmosphere. The solution turned black upon addition of 1 mmol of superhydride solution. The solution was transferred to a stainless-steel pressure vessel which was equipped to an external high-pressure Ar source (Taiatsu Techno Co. Ltd.). The inner pressure of the vessel was first raised to 0.5 MPa using pressurized pure Ar gas (99.9999%), and then the vessel was placed in an oil bath to keep the temperature at 200 °C. The solution in the vessel was continuously stirred for 2 h with a magnetic spin bar. After 2 h, the vessel was removed from the oil bath, cooled to room temperature, and transferred to a glovebox which was filled with purified Ar gas (O_2 and H_2O concentrations < 0.1 ppm). A black, turbid solution in the vessel was transferred to a centrifuge tube without exposed to air and centrifuged at 6000 rpm for 10 min to precipitate black, fine powder. The product powder was washed with diglyme and hexane three times each without being exposed to air and dried under vacuum. The product was finally annealed for 15 h at 500 °C under vacuum to get Zr–Pt alloy NPs. The Zr–Pt alloy NPs converted to cubic $ZrPt_3$ NPs upon 15 h vacuum annealing at 900 °C. *c*-$ZrPt_3$ NPs structurally converted to *h*-$ZrPt_3$,when annealed at 1000 °C for 20 h under vacuum.

2.2.2. Synthesis of Bulk $ZrPt_3$. Polycrystalline bulk samples of intermetallic $ZrPt_3$ were synthesized with an arc furnace in a pure Ar atmosphere (99.9999%). Prior to the synthesis, the arc furnace was evacuated to a vacuum level lower than 10 mPa and backfilled with pure Ar. All the starting materials were purchased from Furuya Kinzoku Co. An aliquot of 1 g of Pt powder (99.9%) was pelletized with a stainless-steel die and melted with the arc furnace into an ingot. Zr (ingot, 99%) was used as received. The ingots of Zr and Pt were weighed such that the molar ratio was Zr:Pt = 1:3 and melted together in the arc furnace to obtain the desired intermetallic $ZrPt_3$. The final product was finally annealed in vacuum at 1000 °C for 72 h.

2.2.3. Powder X-ray Diffractometry (pXRD). Powder X-ray diffractometry (*p*XRD) was performed using Cu Kα radiation (Panalytical X'Pert PRO; λ = 0.1548 nm) with an increment of 0.02 degrees in a range of diffraction angles from 20 to 80 degrees. An obliquely finished Si crystal (nonreflection Si plate) was used as a sample holder to minimize the background.

2.2.4. Hard X-ray Photoemission Spectroscopy (HX-PES). Hard X-ray photoemission spectroscopy (HX-PES) was performed using an X-ray with photon energy of 5.95 keV at BL15XU of SPring-8, Japan. Sample powder was first dispersed in THF in air and dropped onto a carbon substrate. The sample was thoroughly dried in air and transferred into an ultrahigh-vacuum (UHV) chamber equipped with a high-resolution electron spectrometer (VG Vacuum Generator, Scienta R4000). The binding energy of photoelectrons was referenced to the Fermi energy of an Au film that was electrically contacted to the sample. Total energy resolution was set to 240 meV.

2.2.5. Transmission Electron Microscopy (STEM/TEM). We used a 200 kV transmission electron microscope (TEM and/or STEM, JEM-2100F, JEOL) equipped with two aberration correctors (CEOS GmbH) for the image- and probe-forming lens systems and an X-ray energy-dispersive spectrometer (JED-2300T, JEOL) for compositional analysis. Both the aberration correctors were optimized to realize the point-to-point resolutions of TEM and scanning transmission electron microscopy (STEM) as 1.3 and 1.1 Å, respectively. A probe convergence angle of 29 mrad and a high-angle annular-dark-field (HAADF) detector with an inner angle greater than 100 mrad were used for HAADF-STEM observation. An ultrahigh-vacuum STEM (UHV-STEM; TECNAI G2) was used to perform microscopic observation of the morphology and particle size of the materials. The samples for UHV-STEM were prepared by dropping a methanol suspension of the sample powder onto a commercial TEM grid coated with a collodion film. The sample was thoroughly dried in vacuum prior to observation.

2.6. Electrochemistry. A glassy carbon (GC) electrode (5 mm in diameter, Hokuto Denko) was polished prior to use with alumina paste (0.06 μm) over a Milli-Q-water-wetted microcloth (Buhler). The GC electrode was rinsed with Milli-Q water and finally dried in air. An aliquot of 4.2 mg of the sample powder was suspended in a mixture of 1745 μL of distilled water, 440 μL of isopropyl alcohol, and 18 μL of a 5% w/w lower aliphatic alcohols–water solution of Nafion (EW: 1100, Aldrich). After sonication for 60 min, the suspension was dropped onto the GC electrode and dried at 60 °C in air. The GC electrode surface was finally coated with 0.29 mg cm^{-2} of the sample powder.

Cyclic voltammetric (CV) measurements were performed using a computer-controlled electrochemical system (HSV-100, Hokuto Denko) in a three-electrode, two-compartment electrochemical cell (main compartment volume =100 mL, PINE). A Pt wire and an Ag/AgCl electrode (4 M KCl solution) were used as the counter electrode and the reference electrode, respectively. All the voltammograms were acquired at room temperature (23 ± 1 °C) and at a potential sweep rate of 10 mVs^{-1}.The electrochemical surface area (ECSA) of the

sample was determined by adsorption/desorption of hydrogen between −0.16 and +0.2 V, assuming 210 μCcm^{-2} for a monolayer of adsorbed hydrogen on the platinum surface.

Before performing the electro-oxidation of ethanol/formic acid (EtOH/HCOOH, Wako), background currents were first measured in a deaerated 0.5 M aqueous solution of sulfuric acid (H_2SO_4, Wako). The electro-oxidation of ethanol was then carried out in aqueous solutions of 1.0 M EtOH/0.5 M H_2SO_4 and 1.0 M HCOOH/0.5 M H_2SO_4, respectively. The solutions were deaerated with pure Ar gas for 30 min in prior to the measurements.

2.6. Theoretical Calculations. Electronic structure calculations for cubic and hexagonal $ZrPt_3$ were performed on the basis of density-functional theory. The exchange-correlation energy functional was represented by the generalized gradient approximation proposed by Perdew−Burke−Ernzerhof.[31] Projector-augmented wave pseudopotentials were employed as implemented in the VASP code.[32] The valence configurations of the pseudopotentials were $5d^9\ 6s^1$ for Pt and $4d^2\ 5s^2$ for Zr. The energy cutoff for the plane-wave basis set expansion was set at 500 eV. Monkhorst−Pack k-point sets of 10 × 10 × 10 were used for a 4-atom unit cell of cubic $ZrPt_3$ (space group $Fm\bar{3}m$), whereas 8 × 8 × 8 set was used for the 16-atom unit cell of hexagonal $ZrPt_3$ (space group $P63/mmc$). The optimized lattice parameters are as follows a = 4.05 Å for cubic $ZrPt_3$ and a = 5.73 Å, b = 5.73 Å, c = 9.35 Å, β = 120.00° for hexagonal $ZrPt_3$.

The unit cells were extended for the creation of surface models of cubic $ZrPt_3$ (111) and hexagonal $ZrPt_3$ (001). Our slab model of $ZrPt_3$ (111) consists of 15 layers including 120 atoms in total. The seventh−ninth layers were fixed during relaxations of surface geometries in order for representing a bulk region. While a slab model of $ZrPt_3$ (001) consists of 11 layers of $ZrPt_3$ planes including 88 atoms in total. The fifth−eighth layers were fixed during the surface relaxations. In both cases, the thickness of a vacuum layer was set to 10 Å. For the surface calculations, k-point sampling was set at 2 × 2 × 1. Atomic positions of the slab modes were fully relaxed except for the fixed layers until the residual force on each atom was converged to less than 0.02 eV/Å. Similarly, we have also performed calculations of Pt (111) for comparison.

The surface energy (γ) was calculated from the following formula.

$$\gamma = (E_{slab} - NE_{bulk})/(2A)$$

where E_{slab} is the total energy of the slab and E_{bulk} is a total energy of the bulk per unit. N and A are the number of units included in the slab and the surface area, respectively.

3. RESULTS AND DISCUSSION

Figure 1A and B (Figures S1 and S2) shows the pXRD profiles for the $ZrPt_3$ NPs annealed at different temperatures. The pXRD profile for the $ZrPt_3$ NPs annealed at 900 °C is consistent with a simulated reflection pattern for the cubic $CuAu_3$-type structure, indicating that the $ZrPt_3$ NPs were atomically ordered in the $CuAu_3$-type structure (c-$ZrPt_3$ NPs, see inset for the structural model).[29] The c-$ZrPt_3$ NPs annealed at 1000 °C showed a pXRD profile that matches with a simulated pattern for a hexagonal $TiNi_3$-type structure (h-$ZrPt_3$ NPs, see inset for the structural model).[30] The $ZrPt_3$ NPs are transformed from the cubic $CuAu_3$-type- to the hexagonal $TiNi_3$-type structures at temperatures between 900 and 1000 °C. It is notable that the average interatomic distance between Zr and the nearest-neighbor Pt atoms in the h-$ZrPt_3$ NPs, 0.2815 nm, is shorter than that in the c-$ZrPt_3$ NPs, 0.2841 nm. The shorter Zr−Pt bond in the h-$ZrPt_3$ NPs indicates that chemical bond between Zr- and Pt atoms are stronger in the h-$ZrPt_3$ NPs than that in the c-$ZrPt_3$ NPs.

Hard X-ray photoemission spectroscopy using synchrotron radiation (HX-PES; photon energy = 5.95 keV) was performed to further investigate the chemical state of the $ZrPt_3$ NPs (Figure 2A and B and Figure S3).[33−35] Figure 2A presents the

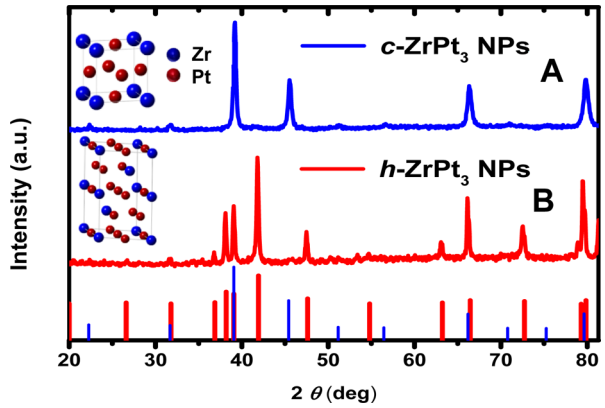

Figure 1. (A) pXRD pattern of the c-$ZrPt_3$ NPs, annealed at 900 °C and (B) pXRD pattern of the h-$ZrPt_3$ NPs, annealed at 1000 °C. Simulated pXRD peaks for hexagonal (red lines) and cubic (blue lines) $ZrPt_3$ are shown by solid markers at the bottom. The inset shows the unit cells of c-$ZrPt_3$ and h-$ZrPt_3$ (where blue balls denote Zr and red balls denote Pt atoms).

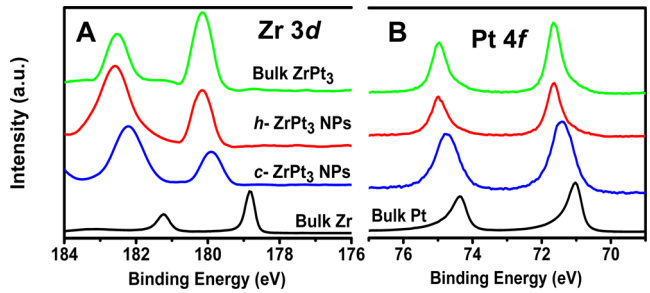

Figure 2. (A and B) HX-PES spectra of the c-$ZrPt_3$ and h-$ZrPt_3$ NPs in the Zr 3d and Pt 4f regions, respectively. HX-PES spectra of bulk Pt, bulk Zr, and bulk $ZrPt_3$ are also shown as a reference.

photoemission spectra in the Zr 3d region. The bulk $ZrPt_3$ and h-$ZrPt_3$ NPs showed Zr $3d_{5/2}$ and $3d_{3/2}$ photoemission peaks at 180.15 ± 0.20 and 182.53 ± 0.20 eV, respectively, which +1.2 eV shifted toward high binding energies with respect to the corresponding peaks for elemental Zr, 178.83 ± 0.20 and 181.23 ± 0.20 eV, respectively. The observed shift in the Zr 3d emission peaks is attributed to the formation of chemical bonds between Zr and Pt, which weakens the charge screening of the Zr 3d core hole to increase the binding energy of core emissions.[36] By contrast, the Zr 3d emission peaks for the c-$ZrPt_3$ NPs, which were situated at 179.90 ± 0.20 and 182.22 ± 0.20 eV, exhibited a +1.0 eV shift with respect to those of the reference Zr metal. This binding-energy shift in the Zr 3d emissions for the c-$ZrPt_3$ NPs is 20% smaller than that for the h-$ZrPt_3$ NPs or bulk $ZrPt_3$. The Zr−Pt bonds in the c-$ZrPt_3$ NPs are, as indicated by the structural analysis on the pXRD data, weaker than those in the h-$ZrPt_3$ NPs or bulk $ZrPt_3$. The formation of Zr−Pt bonds also increases the binding energies of the Pt-core emissions from the $ZrPt_3$ materials (Figure 2B). The bulk $ZrPt_3$ and the h-$ZrPt_3$ NPs showed the Pt $4f_{7/2}$ and $4f_{5/2}$ photoemission peaks at 71.61 ± 0.20 and 74.96 ± 0.20 eV, respectively, which shifted by +0.58 eV toward high binding energies with respect to the corresponding peaks for bulk Pt, 71.03 ± 0.20 and 74.38 ± 0.20 eV, respectively. The Pt 4f emission peaks for the c-$ZrPt_3$ NPs, which were situated at 71.41 ± 0.20 and 74.76 ± 0.20 eV, exhibited a smaller shift, +0.38 eV with respect to those for bulk Pt. This small binding-energy shift in the Pt core emissions confirms that the Zr−Pt

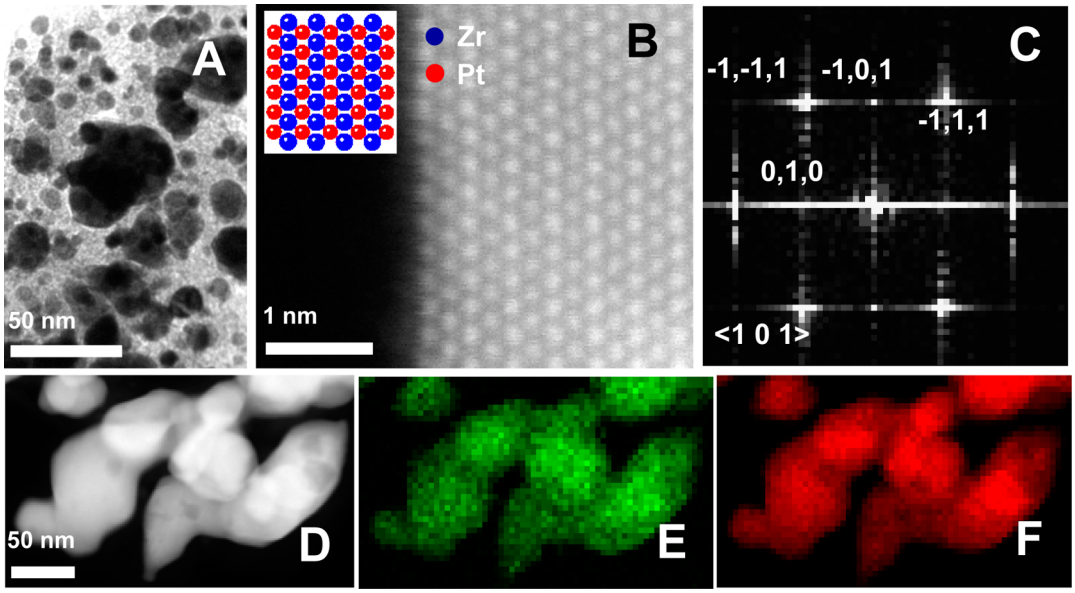

Figure 3. (A) TEM image, (B) HAADF-STEM image, and (C) FFT pattern of part B. (D) STEM image and corresponding EDS mapping of the *c*-$ZrPt_3$ NPs for (E) Pt and (F) Zr.

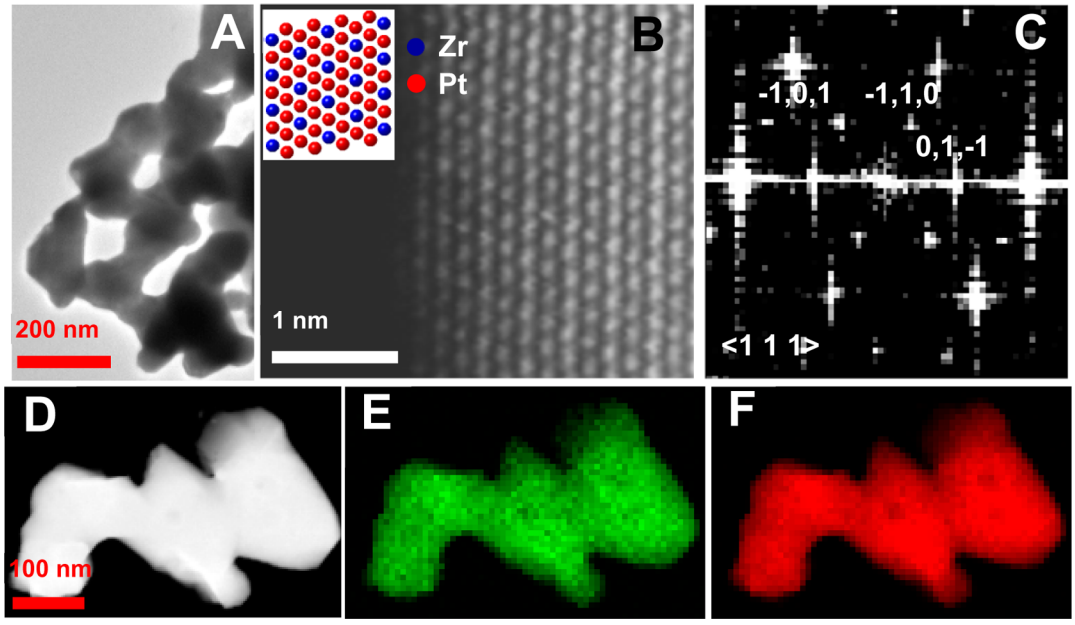

Figure 4. (A) TEM image, (B) HAADF-STEM image, (C) FFT pattern of part B. (D) STEM image and corresponding EDS mapping of the *h*-$ZrPt_3$ NPs for (E) Pt and (F) Zr.

bonds in the *c*-$ZrPt_3$ NPs are weaker than those in the *h*-$ZrPt_3$ NPs.

Figure 3A presents a transmission electron microscopy (TEM) image of *c*-$ZrPt_3$ NPs, of which average particle size was around 100 nm. The high-angle annular dark field (HAADF) image of the *c*-$ZrPt_3$ NPs (Figure 3B) and the corresponding fast Fourier-transformation pattern (FFT, Figure 3C) are consistent with the atomic arrangement expected for the cubic $AuCu_3$-type structure. The scanning-transmission electron microscopy (STEM) image, accompanied by compositional mapping for Zr and Pt, demonstrates uniform distribution of Zr and Pt over the NPs in a mole ratio, Zr:Pt = 23.1:76.9 as expected for $ZrPt_3$ (Figure 3D−F, Figure S4). Figure 4A presents the STEM image of the *h*-$ZrPt_3$ NPs, which had an average particle size less than 200 nm. The HAADF/STEM images (Figure 4B) and the corresponding FFT pattern (Figure 4C) indicate that the Zr and Pt atoms are arranged in the $TiNi_3$-type structure. Compositional mapping and STEM images demonstrate the uniform distribution of Zr and Pt over the *h*-$ZrPt_3$ NPs in the expected mole ratio, Zr:Pt = 25.3:74.7 (Figure 4D−F, Figure S5). Moreover, detailed FFT analysis at different areas of the high-resolution STEM images (Figure S6) has demonstrated that the surface atomic arrangement of the *c*-$ZrPt_3$ NPs and of the *h*-$ZrPt_3$ was identical to that in the bulk, showing that the surface of the NPs are free from Pt-skin. Based on the *p*XRD and TEM/STEM characterization, we conclude that both the *c*-$ZrPt_3$ and *h*-$ZrPt_3$ NPs are uniformly consisted of Zr and Pt at the molar ratio of

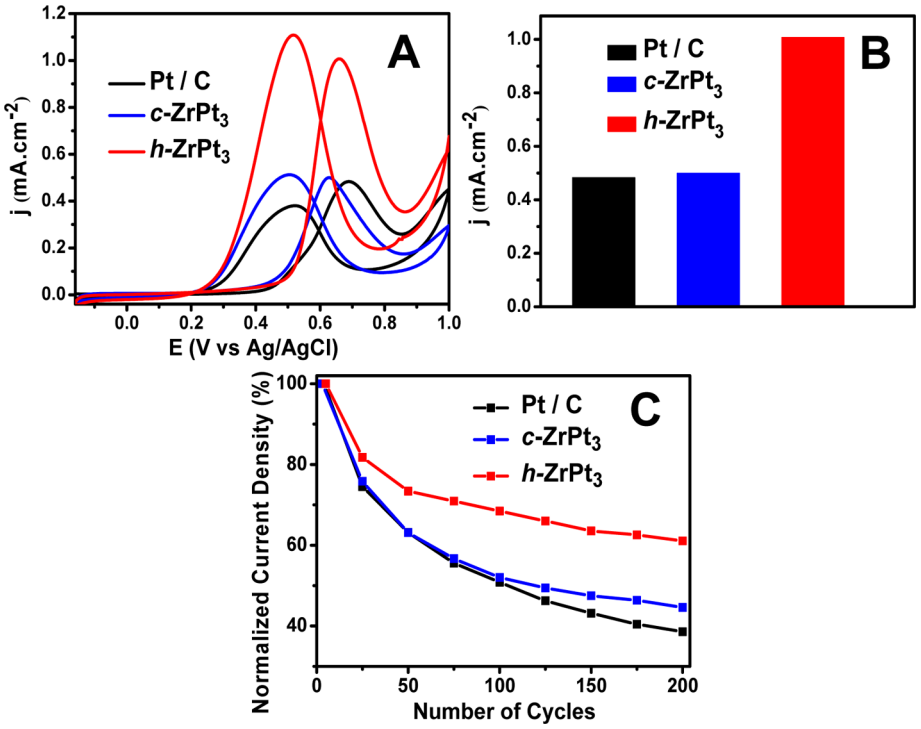

Figure 5. (A) Ethanol oxidation polarization curves for Pt/C and *c*-$ZrPt_3$ and *h*-$ZrPt_3$ NPs in 1 M ethanol/0.5 M H_2SO_4 solution at a scan rate of 10 mV s^{-1}. (B) Summary of the specific activities for ethanol electro-oxidation at the peak potentials. (C) Normalized current densities for ethanol electrooxidation as functions of number of potential cycles.

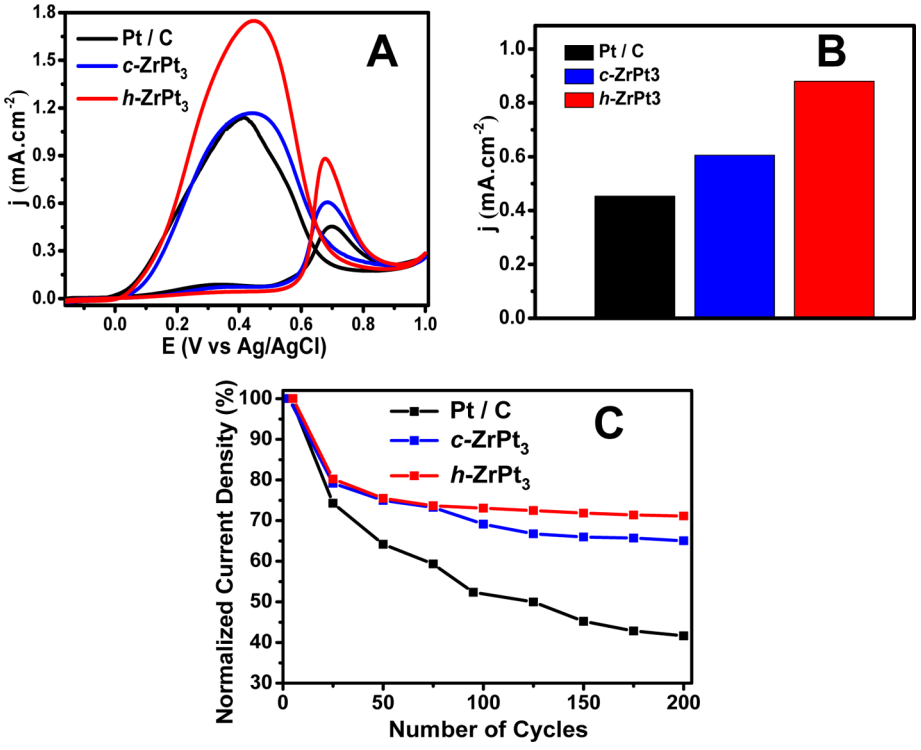

Figure 6. (A) Formic acid oxidation for Pt/C and *c*-$ZrPt_3$ and *h*-$ZrPt_3$ NPs in 1 M formic acid/0.5 M H_2SO_4 solution at a scan rate of 10 mV s^{-1}. (B) Comparison of the specific activities for formic electro-oxidation at the peak potentials. (C) Normalized current densities for formic acid electrooxidation as functions of number of potential cycles.

Zr:Pt = 1:3, but ordered in the different $AuCu_3$-type and $TiNi_3$-type structures, respectively. The difference in the bulk structure, as elucidated by structural analysis and HX-PES, results in the different strength of Zr−Pt bonds: the Zr−Pt bonds in the *h*-$ZrPt_3$ NPs are stronger than those in the *c*-$ZrPt_3$ NPs.

Electrochemical activity and long-term stability for the oxidation of ethanol and formic acid were investigated for

dx.doi.org/10.1021/am504147q | *ACS Appl. Mater. Interfaces* 2014, 6, 16124−16130

commercial carbon-supported Pt NPs (Pt/C, E-TEK), the *c*-$ZrPt_3$ NPs and *h*-$ZrPt_3$ NPs. All the electrochemical measurements were performed at room temperature in 0.5 M H_2SO_4 aqueous solution which contained 1 M of fuel. Figure 5A shows the cyclic voltammographs (CV) for ethanol electro-oxidation over the different catalysts. All the currents, which correspond to the 10th cycle of the CV, are normalized to the calculated ECSA (Figure S8). The electro-oxidation peaks on the anodic scan for the *c*-$ZrPt_3$ NPs were slightly more intense than the corresponding peaks for the Pt/C, showing slight enhancement in the electrocatalytic activity. By vast contrast, the electro-oxidation peak for the *h*-$ZrPt_3$ NPs were 2-fold more intense than the corresponding peak for the *c*-$ZrPt_3$ NPs or Pt/C, demonstrating significantly enhanced catalytic activity of the *h*-$ZrPt_3$ NPs (Figure 5B). Figure 5C shows the results of durability tests on the different catalysts. The current densities at the peak maxima for the Pt/C and *c*-$ZrPt_3$ NPs diminished by 72% and 66%, respectively, after 200 electrochemical cycles. By contrast, the *h*-$ZrPt_3$ NPs showed only a 40% decrease in the current density during the repeated cycles (Figure S9). Moreover, the *h*-$ZrPt_3$ NPs exhibited higher electro-oxidation activity (peak current: 0.886 mA cm^{-2}) than the Pt/C (peak current: 0.455 mA cm^{-2}) or the *c*- $ZrPt_3$ NPs (peak current: 0.611 mA cm^{-2}) (Figures 6A, B) for the electro-oxidation of formic acid. The current density over the *h*-$ZrPt_3$ NPs decreased more slowly during the repeated potential scans than that of the Pt/C and *c*-$ZrPt_3$ NPs. It is demonstrated from the specific-activity plot (Figure 6C, Figure S10) that the *h*-$ZrPt_3$ NPs remained the best catalyst for the electro-oxidation of formic acid in terms of the catalytic activity and durability. The corresponding mass-activity plots are presented in Figure S11.

To investigate the surface-poisoning effect, CO-stripping experiment was carried out at room temperature in 0.5 M H_2SO_4 at a scan rate of 10 mV s^{-1}. The Pt/C NPs exhibited a prominent CO-stripping peak at +0.66 V (Figure 7), whereas

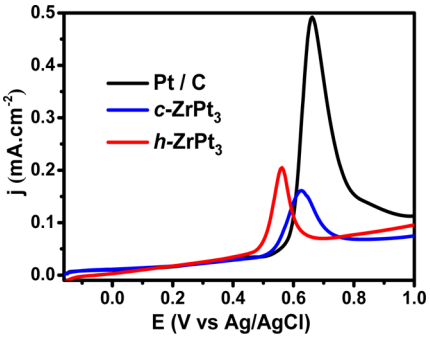

Figure 7. CO stripping profiles of Pt/C and *c*-$ZrPt_3$ and *h*-$ZrPt_3$ NPs in 0.5 M aqueous H_2SO_4 solution at a scan rate of 10 mV s^{-1}.

the *c*-$ZrPt_3$ NPs and *h*-$ZrPt_3$ NPs exhibited peaks at +0.62 and +0.56 V, respectively. The onset potential of CO-stripping for the *h*-$ZrPt_3$ NPs was lower than those for the *c*-$ZrPt_3$ NPs and Pt/C, demonstrating that the *h*-$ZrPt_3$ NPs are tolerant to CO poisoning.

HX-PES and *p*XRD analysis have shown that the Zr−Pt bonds in the *h*-$ZrPt_3$ NPs are stronger than in *c*-$ZrPt_3$ NPs, which in turn results in the increased surface energy of the *h*-$ZrPt_3$ NPs. Indeed, computational calculations have supported that the surface energy of the most-stable facet of the *h*-$ZrPt_3$ NPs, 1.47 J m^{-2}, is higher than those of the *c*-$ZrPt_3$ NPs, 1.34 J m^{-2}. It is widely known that metal NPs with high-energy surfaces exhibit high catalytic performance.[37−39] The observed enhancement in the electro-oxidation activity of the *h*-$ZrPt_3$ NPs may be attributed to the increased surface energy, which may promote adsorption/decomposition of ethanol/formic acid molecules on the surface. Importantly, this increase in the surface energy of the *h*-$ZrPt_3$ NPs is compensated by lowering in the bulk free energy, retaining the stability of the catalyst: the amplitude of the formation enthalpy for the *h*-$ZrPt_3$, ΔH_f = −100.8 kJ mol^{-1} of Zr, is larger than that for the *c*-$ZrPt_3$, ΔH_f = −99.8 kJ mol^{-1} of Zr.[40]

CONCLUSION

In conclusion, we have successfully synthesized differently ordered $ZrPt_3$ NPs with the cubic $CuAu_3$-type structure (*c*-$ZrPt_3$ NPs) and the hexagonal $TiNi_3$-type structure (*h*-$ZrPt_3$ NPs) by promoting bulk-structural transformation through controlled annealing. It was demonstrated that the *h*-$ZrPt_3$ NPs exhibit better catalytic performance than the *c*-$ZrPt_3$ NPs, in terms of the enhanced electro-oxidation activity toward ethanol/formic acid and improved stability to repeated electrochemical cycles. The enhanced catalytic performance of the *h*-$ZrPt_3$ NPs originates from the bulk-structural transformation from the cubic to the hexagonal structures, which elevates the surface energy in compensation for the lowering in bulk free energy. The successful development of the $ZrPt_3$ NPs will open up a new route to bulk-structure-tailored metal catalysts, which may compromise the mutually exclusive properties desired for catalysts: the high surface energy for high catalytic activity and the low bulk free energy for long-term stability.

ASSOCIATED CONTENT

Supporting Information

Synthesis, characterization (pXRD, HX-PES, TEM), and electrochemical data. This material is available free of charge via the Internet at http://pubs.acs.org.

AUTHOR INFORMATION

Corresponding Authors

*E-mail: GUBBALA.Venkataramesh@nims.go.jp (G.V.).
*E-mail: ABE.Hideki@nims.go.jp (H.A.).

Notes

The authors declare no competing financial interest.

ACKNOWLEDGMENTS

This work was preliminarily supported by the JST PRESTO program, the Ministry of Education, Culture, Sports, Science and Technology (MEXT) and the Japan Society for the Promotion of Science (JSPS) through Grant-in-Aid 23560855. The HX-PES measurements at BL15XU of SPring-8 were performed under the approval of the Synchrotron X-ray Station (Proposal No. 2012B4609, 2013A4600, 2013B4602). The authors are grateful to HiSOR, Hiroshima University, and JAEA/SPring-8 for the development of HX-PES at BL15XU of SPring-8.

REFERENCES

(1) Page, K. A.; Rowe, B. W. An Overview of Polymer Electrolyte Membranes for Fuel Cell Applications. *ACS Sym. Sers.* **2012**, *1096*, 147−164.

(2) Warren, S. C.; Thimsen, E. Plasmonic Solar Water Splitting. *Energy Environ. Sci.* **2012**, *5*, 5133−5146.
(3) Cui, C.-H.; Yu, S.-H. Engineering Interface and Surface of Noble Metal Nanoparticle Nanotubes toward Enhanced Catalytic Activity for Fuel Cell Applications. *Acc. Chem. Res.* **2013**, *46*, 1427−1437.
(4) Steele, B. C. H.; Heinzel, A. Materials for Fuel-cell Technologies. *Nature* **2001**, *414*, 345−352.
(5) Mehta, V.; Cooper, J. S. Review and Analysis of PEM Fuel Cell Design and Manufacturing. *J. Power Sources* **2003**, *114*, 32−53.
(6) Litster, S.; McLean, G. PEM Fuel Cell Electrodes. *J. Power Sources* **2004**, *130*, 61−76.
(7) Kowal, A.; Li, M.; Shao, M.; Sasaki, K.; Vukmirovic, M. B.; Zhang, J.; Marinkovic, N. S.; Liu, P.; Frenkel, A. I.; Adzic, R. R. Ternary Pt/Rh/SnO_2 Electrocatalysts for Oxidizing Ethanol to CO_2. *Nat. Mater.* **2009**, *8*, 325−330.
(8) Stephens, I. E. L.; Bondarenko, A. S.; Grønbjerg, U.; Rossmeisl, J.; Chorkendorff, I. Understanding the Electrocatalysis of Oxygen Reduction on Platinum and Its Alloys. *Energy Environ. Sci.* **2012**, *5*, 6744−6762.
(9) Kang, Y.; Pyo, J. B.; Ye, X.; Gordon, T. R.; Murray, C. B. Synthesis, Shape Control, and Methanol Electro-oxidation Properties of Pt-Zn Alloy and Pt_3Zn Intermetallic Nanocrystals. *ACS Nano* **2012**, *6*, 5642−5647.
(10) Wang, D.; Xin, H. L.; Hovden, R.; Wang, H.; Yu, Y.; Muller, D. A.; DiSalvo, F. J.; Abruña, H. D. Structurally Ordered Intermetallic Platinum−cobalt Core−shell Nanoparticles with Enhanced Activity and Stability as Oxygen Reduction Electrocatalysts. *Nat. Mater.* **2013**, *12*, 81−87.
(11) Stamenkovic, V. R.; Fowler, B.; Mun, B. S.; Wang, G.; Ross, P. N.; Lucas, C. A.; Markovic, N. M. Improved Oxygen Reduction Activity on $Pt_3Ni(111)$ via Increased Surface Site Availability. *Science* **2007**, *315*, 493−497.
(12) Herranz, T.; Ibáñez, M.; Gómez de la Fuente, J. L.; Pérez-Alonso, F. J.; Peña, M. A.; Cabot, A.; Rojas, S. In Situ Study of Ethanol Electrooxidation on Monodispersed Pt3Sn Nanoparticles. *CHEMELECTROCHEM* **2014**, *1*, 885−895.
(13) Alayoglu, S.; Zavalij, P.; Eichhorn, B.; Wang, Q.; Frenkel, A. I.; Chupas, P. Structural and Architectural Evaluation of Bimetallic Nanoparticles: a Case Study of Pt-Ru Core-shell and Alloy Nanoparticles. *ACS Nano* **2009**, *3*, 3127−3137.
(14) Xu, D.; Liu, Z.; Yang, H.; Liu, Q.; Zhang, J.; Fang, J.; Zou, S.; Sun, K. Solution-Based Evolution and Enhanced Methanol Oxidation Activity of Monodisperse Platinum−Copper Nanocubes. *Angew. Chem., Int. Ed.* **2009**, *48*, 4217−4221.
(15) Abe, H.; Matsumoto, F.; Alden, L. R.; Warren, S. C.; Abruña, D. H.; DiSalvo, F. J. Electrocatalytic Performance of Fuel Oxidation by Pt_3Ti Nanoparticles. *J. Am. Chem. Soc.* **2008**, *130*, 5452−5458.
(16) Kang, Y.; Murray, C. B. Synthesis and Electrocatalytic Properties of Cubic Mn−Pt Nanocrystals (Nanocubes). *J. Am. Chem. Soc.* **2010**, *132*, 7568−7569.
(17) Porter, N. S.; Wu, H.; Quan, Z.; Fang, J. Shape-Control and Electrocatalytic Activity-Enhancement of Pt-Based Bimetallic Nanocrystals. *Acc. Chem. Res.* **2013**, *46*, 1867−1877.
(18) Huang, X. Q.; Zhao, Z. P.; Fan, J. M.; Tan, Y. M.; Zheng, N. F. Amine-Assisted Synthesis of Concave Polyhedral Platinum Nanocrystals Having {411} High-Index Facets. *J. Am. Chem. Soc.* **2011**, *133*, 4718−4721.
(19) Kang, Y. J.; Qi, L.; Li, M.; Diaz, R. E.; Su, D.; Adzic, R. R.; Stach, E.; Li, J.; Murray, C. B. Highly Active Pt_3Pb and Core−Shell Pt_3Pb−Pt Electrocatalysts for Formic Acid Oxidation. *ACS Nano* **2012**, *6*, 2818−2825.
(20) Furukawa, S.; Suga, A.; Komatsu, T. Highly Efficient Aerobic Oxidation of Various Amines using Pd_3Pb Intermetallic Compounds as Catalysts. *Chem. Commun.* **2014**, *50*, 3277−3280.
(21) Komatsu, T.; Takasaki, K.; Ozawa, S.; Furukawa, S.; Muramatsu, A. PtCu Intermetallic Compound Supported on Alumina Active for Preferential Oxidation of CO in Hydrogen. *J. Phys. Chem. C* **2013**, *117*, 10483−10491.
(22) Casado-Rivera, E.; Volpe, D. J.; Alden, L.; Lind, C.; Downie, C.; Vázquez-Alvarez, T.; Angelo, A. C. D.; DiSalvo, F. J.; Abruña, H. D. Electrocatalytic Activity of Ordered Intermetallic Phases for Fuel Cell Applications. *J. Am. Chem. Soc.* **2004**, *126*, 4043−4049.
(23) Ramesh, G. V.; Kodiyath, R.; Tanabe, T.; Manikandan, M.; Fujita, T.; Matsumoto, F.; Ishihara, S.; Ueda, S.; Yamashita, Y.; Ariga, K.; Abe, H. $NbPt_3$ Intermetallic Nanoparticles: Highly Stable and CO-Tolerant Electrocatalyst for Fuel Oxidation. *CHEMELECTROCHEM* **2014**, *1*, 728−732.
(24) Sato, A.; Chishima, E.; Soma, K.; Mori, T. Shape Memory Effect in $\gamma \rightleftarrows \epsilon$ Transformation in Fe-30Mn-1Si Alloy Single Crystals. *Acta Metall.* **1982**, *30*, 1177−1183.
(25) Benafan, O.; Padula, S. A., II; Noebe, R. D.; Sisneros, T. A.; Vaidyanathan, R. Role of B19′ Martensite Deformation in Stabilizing Two-way Shape Memory Behavior in NiTi. *J. Appl. Phys.* **2012**, *112*, 093510 (1−11).
(26) Yamauchi, K.; Ohkata, I.; Tsuchiya, K.; Miyazaki, S. *Shape Memory and Superelastic Alloys: Applications and Technologies*; Woodhead publishing limited: Cambridge, 2011.
(27) Favier, F.; Walter, E. C.; Zach, M. P.; Benter, T.; Penner, R. M. Hydrogen Sensors and Switches from Electrodeposited Palladium Mesowire Arrays. *Science* **2001**, *293*, 2227−2231.
(28) Terayama, A.; Nagai, K.; Kyogoku, H. Fabrication of Ti-Ni-Zr Shape Memory Alloy by P/M Process. *Materials Transactions* **2009**, *50*, 2446−2450.
(29) Panday, P. K.; Frank, K.; Biswas, T. K.; Bhan, S.; Schubert, K. Einige Strukturdaten metallischer Phasen. *Naturwissenschaften* **1968**, *55*, 542−543.
(30) Raman, A.; Schubert, K. Structural Investigations on Some Alloy Systems Homologous and Quasi-Homologous toT^4 −T^9. *Z. Metallkd.* **1964**, *55*, 704−710.
(31) Perdew, P. J.; Burke, K.; Ernzerhof, M. Generalized Gradient Approximation Made Simple. *Phys. Rev. Lett.* **1996**, *77*, 3865−3868.
(32) Kresse, G.; Furthmüller, J. Efficient Iterative Schemes for Ab Initio Total-energy Calculations Using a Plane-wave Basis Set. *Phys. Rev. B* **1996**, *54*, 11169−11186.
(33) Ohsawa, T.; Ohashi, N.; Adachi, Y.; Sakaguchi, I.; Ryoken, H.; Matsumoto, K.; Haneda, H.; Ueda, S.; Yoshikawa, H.; Kobayashi, K. Hard X-ray Photoemission Spectroscopy in Wrutzite-type Zinc Magnesium Oxide Solid-solution Films Grown by Pulsed-laser Deposition. *Appl. Phys. Lett.* **2008**, *92*, 232108 (1−3).
(34) Ohsawa, T.; Adachi, Y.; Sakaguchi, I.; Matsumoto, K.; Haneda, H.; Ueda, S.; Yoshikawa, H.; Kobayashi, K.; Ohashi, N. Electronic States in Zinc Magnesium Oxide Alloy Semiconductors: Hard X-ray Photoemission Spectroscopy and Density Functional Theory Calculations. *Chem. Mater.* **2009**, *21*, 144−150.
(35) Ueda, S.; Katsuya, Y.; Tanaka, M.; Yoshikawa, H.; Yamashita, Y.; Ishimaru, S.; Matsushita, Y.; Kobayashi, K. Present Status of the NIMS Contract Beamline BL15XU at SPring-8. *AIP Conference Proceedings*; 2010; pp 403−406; 10.1063/1.3463225
(36) Wakisaka, M.; Mitsui, S.; Hirose, Y.; Kawashima, K.; Uchida, H.; Watanabe, M. Electronic Structures of Pt−Co and Pt−Ru Alloys for CO-Tolerant Anode Catalysts in Polymer Electrolyte Fuel Cells Studied by EC−XPS. *J. Phys. Chem. B* **2006**, *110*, 23489−23496.
(37) Tian, N.; Zhou, Z. Y.; Sun, S. G.; Ding, Y.; Wang, Z. L. Synthesis of Tetrahexahedral Platinum Nanocrystals with High-index Facets and High Electro-oxidation Activity. *Science* **2007**, *316*, 732−735.
(38) Tian, N.; Zhou, Z. Y.; Sun, S. G. Platinum Metal Catalysts of High-Index Surfaces: From Single-Crystal Planes to Electrochemically Shape-Controlled Nanoparticles. *J. Phys. Chem. C* **2008**, *112*, 19801−19817.
(39) Tian, N.; Zhou, Z. Y.; Sun, S. G. Electrochemical Preparation of Pd Nanorods with High-index Facets. *Chem. Commun.* **2009**, 1502−1504.
(40) Xing, W.; Chen, X.-Q.; Li, D.; Li, Y.; Fu, C. L.; Meschel, S. V.; Ding, X. First-principles Studies of Structural Stabilities and Enthalpies of Formation of Refractory Intermetallics: TM and TM_3 (T = Ti, Zr, Hf; M = Ru, Rh, Pd, Os, Ir, Pt). *Intermetallics* **2012**, *28*, 16−24.